Predictive modeling of nanoscale domain morphology in solution-processed organic thin films

Cyrus Schaaf,[1] Michael Jenkins,[1] Robell Morehouse,[1] Dane Stanfield,[1] Stephen McDowall,[2]
Brad L. Johnson,[3] and David L. Patrick[1,*]

[1]*Department of Chemistry, Western Washington University, 516 High Street, Bellingham, Washington 98225, USA*
[2]*Department of Mathematics, Western Washington University, 516 High Street, Bellingham, Washington 98225, USA*
[3]*Department of Physics, Western Washington University, 516 High Street, Bellingham, Washington 98225, USA*

The electronic and optoelectronic properties of molecular semiconductor thin films are directly linked to their extrinsic nanoscale structural characteristics such as domain size and spatial distributions. In films prepared by common solution-phase deposition techniques such as spin casting and solvent-based printing, morphology is governed by a complex interrelated set of thermodynamic and kinetic factors that classical models fail to adequately capture, leaving them unable to provide much insight, let alone predictive design guidance for tailoring films with specific nanostructural characteristics. Here we introduce a comprehensive treatment of solution-based film formation enabling quantitative prediction of domain formation rates, coverage, and spacing statistics based on a small number of experimentally measureable parameters. The model combines a mean-field rate equation treatment of monomer aggregation kinetics with classical nucleation theory and a supersaturation-dependent critical nucleus size to solve for the quasi-two-dimensional temporally and spatially varying monomer concentration, nucleation rate, and other properties. Excellent agreement is observed with measured nucleation densities and interdomain radial distribution functions in polycrystalline tetracene films. Numerical solutions lead to a set of general design rules enabling predictive morphological control in solution-processed molecular crystalline films.

I. INTRODUCTION

Solution-processed polycrystalline molecular films are increasingly used as active layers in electronic and optoelectronic device applications such as flexible integrated circuits, displays, photovoltaics, actuators, and sensor arrays [1–12]. For these and related applications, optimizing device performance requires careful control over the morphology, size, spatial positioning, and other nanoscale growth characteristics of crystalline domains, which strongly influence charge carrier mobility, trap densities, optical scattering, and other active layer electronic properties [13–22]. In films prepared by spin casting, dip coating, stamping, and related methods, crystallization is typically induced by solvent evaporation, which is used to drive the concentration of dissolved molecular monomers above a critical level, nucleating a film of crystalline precipitates. Under these conditions nucleation is influenced by a combination of interrelated thermodynamic and kinetic factors, including the rate of solvent loss, monomer diffusivity, and the size and monomer concentration dependence of the free-energy barrier to nucleus formation. Classical models treating crystal formation in bulk solution or on bare surfaces in vacuum-deposited films are unable to adequately capture these phenomena, and the current theoretical understanding of crystallization in solution-deposited films is unable to provide much insight, let alone predictive design guidance for tailoring films with specific nanostructural properties [23]. For example, even basic morphological characteristics of solution-processed films, such as the number of crystals nucleated per unit area, their spacing statistics, or size distribution, are generally not possible to predict for a given set of materials and conditions,

but rather must be determined on the basis of trial-and-error experimentation. This represents a major barrier to rational design and selection of new molecular thin-film materials, processing conditions, and applications based on them.

Here we introduce a model for molecular crystallization applicable to solution-processed molecular films enabling quantitative prediction of the time- and chemical potential driving rate-dependent crystal coverage and intercrystalline spacing statistics. Based on a small number of experimentally measureable parameters, we show that the model produces good agreement with observed nucleation densities and interdomain separation radial distribution functions and leads to a set of general design rules useful for guiding the selection of experimental conditions. Our treatment combines mean-field rate equation (MFRE) and competitive diffusion models constructed around a modified version of the classic Walton relation [24] for the nucleation free energy, as well as a concentration-dependent critical nucleus size. The approach can be considered as an adaptation of well-established predictive models, originally developed to treat submonolayer island formation by vacuum deposition [e.g., physical vapor deposition (PVD)], translated to the solution environment. Such an adaptation is possible because vacuum and solution thin-film growth involve fundamentally the same underlying phenomena, namely, a driven time-dependent increase in the monomer supersaturation to induce crystallization, quasi-two-dimensional (2D) growth environments, and dynamic competition for monomers between nucleation and growth. Hence, they should be amenable to treatment by a similar set of principles. The main difference is that the critical nucleus size in solution tends to be much larger than in vacuum and is moreover strongly dependent on monomer concentration, which is itself a dynamic (both spatially and temporally varying) quantity. We account for this by incorporating

*Corresponding author: david.patrick@wwu.edu

corrections to the Walton relation accounting for the supersaturated liquid environment and implementation of a straightforward numerical scheme in the solution of the MFREs enabling on-the-fly computation of the critical nucleus size. The model is shown to provide an accurate description of solution-deposited tetracene (TET) films, including quantitative agreement with the measured induction time, nucleation rate, number of crystals formed per unit substrate area, and their spacing statistics. The resulting findings represent a step toward the development of the first generally applicable, predictive model of nanoscale domain morphology in solution-processed molecular crystalline films.

II. MODELING THE NUCLEATION RATE

We begin by considering the time evolution of the number of crystals formed per unit volume of solution (crystal density N) as the monomer chemical potential $\mu_1(t)$ is driven toward and ultimately beyond a critical level inducing crystallization. Here $N(t)$ is a central quantity governing film structure; it determines the average domain size at high coverage (~ 1 ML) and is connected to the crystal size distribution and spacing statistics at all coverages. The method for driving $\mu_1(t)$ may vary depending on the experimental details, via including solvent evaporation, a reduction in temperature of a saturated solvent, or introduction of an antisolvent. Here we explicitly consider the situation where $\mu_1(t)$ is driven via the continual addition of new monomers to a quasi-2D liquid solvent layer having fixed volume, temperature, and pressure. This is the situation represented by our experimental system, in which fresh monomers are continually and uniformly added to a thin liquid solvent layer coating a glass substrate at a constant flux rate F (monomers $\mu m^{-3} s^{-1}$). New monomers are carried by a gas flow impinging on the surface of the solvent layer, which undergoes negligible evaporation due to its low vapor pressure. Once a monomer impinges on and dissolves into the solvent it is assumed to be irreversibly trapped in the liquid. It is important to note that, within the context of our model, at an early stage of film formation this method of driving $\mu_1(t)$ is functionally equivalent to evaporating solvent from a saturated solution at a fixed rate; here monomers are added to a fixed initial solvent volume, rather than fixing the initial number of monomers and decreasing the volume. We choose this organic vapor-liquid-solid deposition method because it enables greater experimental control over the driving rate $d\mu_1(t)/dt$, it produces large high-quality crystallites suitable for device applications, and it enables growth of molecular films from compounds of even very low solubility [25].

Crystal formation and the addition and loss of monomers to/from solution can be treated using a set of coupled mean-field rate equations governing the concentrations of monomers n and crystals N [26]:

$$\frac{dn}{dt} = F - K P(i^*, n) n - K n N, \qquad (1a)$$

$$\frac{dN}{dt} = K P(i^*, n) n. \qquad (1b)$$

Here K ($m^3 s^{-1}$) is a collision/capture kernel for the rate of uptake of monomers by crystals and $P(i^*, n)$ is the concen-

tration of aggregates of size i^* at concentration n, where i^* is one monomer less than the critical nucleus size. We model the collision kernel with a Smoluchowski function for diffusion-limited coalescence of spherical particles with diffusivity D : $K = \gamma 4\pi(a + ai^{*\frac{1}{3}})(D + Di^{*-\frac{1}{3}}) \approx \gamma 4\pi ai^{*\frac{1}{3}} D$, where γ is a unitless parameter used to correct for microscopic processes that have been omitted from the full kernel, such as the effects of attractive or repulsive intermolecular forces on the aggregation rate [27], and a is the radius of a TET molecule. We derive the function $P(i^*, n)$ from the free-energy change for the formation of aggregates of size i^* in the solvent, which is given by [28,29]

$$\Delta G_i(n) = -(i-1)kT \ln(n/n_0) + 4\pi \sigma a^2(i^{\frac{2}{3}} - 1). \qquad (2)$$

The concentration of critical clusters $P(i^*, n) = n \exp[-\frac{\Delta G_i^*}{kT}]$ is then

$$P(i^*, n) = n \left(\frac{n}{n_0}\right)^{i^*-1} \exp\left[\frac{-4\pi \sigma a^2(i^{*\frac{2}{3}} - 1)}{kT}\right], \qquad (3)$$

where n_0 is the equilibrium saturation value of monomers in the solvent, σ is the solid-liquid interfacial energy associated with the formation of the cluster, k is the Boltzmann constant, and T is the solvent temperature. Because temperature is held fixed in our experiment, we omit the temperature dependence of n_0 and D. In our treatment we consider only two cluster sizes, monomers and stable crystals, combining all other cluster sizes into these binary categories. This approach is consistent with dividing the complete (infinite set of) rate equations for clusters of all sizes into subcritical (assumed to be dominated by monomers) and stable sizes and summing over the stable crystals to create a net stable density [30,31]. The units in Eqs. (1) are in volumetric flux, i.e., number per volume per time.

A key feature of this formulation, necessary for the accurate description of crystallization in solution, is that i^* is a function of the monomer concentration [26]. In classic MFRE models treating submonolayer island nucleation in films prepared by PVD, i^* is always assumed constant, independent of the adatom coverage. This approximation is possible when i^* is small ($\leqslant \sim 5$), as is normally the case in vacuum nucleation. However, for molecular crystallization in a liquid solvent, where i^* is much larger ($\gg 10$, discussed below), the assumption $i^* = $ const is no longer adequate. Treating the critical size $i^*(t)$ as a dynamical variable thus distinguishes the present treatment from classic MFRE models of submonolayer island formation in vacuum-deposited films and turns out to be a necessary ingredient to describe nucleation behavior in the liquid environment. Here $i^*(t)$ is derived assuming homogeneous nucleation using classical nucleation theory (CNT) based on the free energy of formation of spherical clusters of size i^* at (supersaturated) concentration n, which gives [26,32]

$$i^*(n) = \left(\frac{8\pi \sigma a^2}{3kT \ln\left(\frac{n}{n_0}\right)}\right)^3. \qquad (4)$$

We note that more sophisticated and potentially more accurate expressions for $i^*(n)$ are available using contemporary theories of nucleation [33], but for the sake of simplicity and
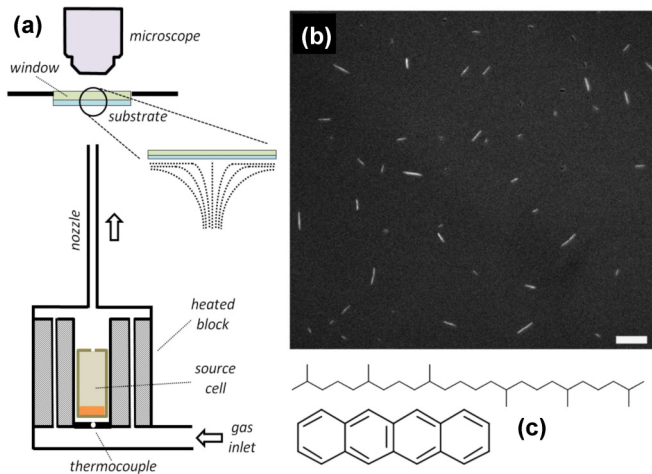
FIG. 1. (a) Schematic of the deposition apparatus. The components are housed inside a sealed nitrogen-filled chamber. TET vapor produced in a heated crucible is carried to a squalane-coated ITO-glass substrate by a stream of gas exiting through a tapered nozzle, impinging with axisymmetric stagnation point flow resulting in uniform deposition over a 1-cm^2 area. The substrate temperature is held fixed by a thermoelectric element. Film growth is monitored *in situ* via fluorescence videomicroscopy through a viewport in the lid. (b) Epifluorescence micrograph showing a representative TET film. The scale bar is 100 μm. (c) Chemical structures of squalane and tetracene.

because the present approach already provides good agreement with experiment, here we use CNT to describe the critical nucleus size and its dependence on supersaturation n/n_0.

Before continuing further with the development of the model, we first examine how well Eqs. (1) agree with experiment. To do so, we studied crystallization of submonolayer 2,3-benzanthracene (TET) films in a thin layer of the organic solvent squalane (2,6,10,15,19,23-hexamethyltetracosane) applied to an indium-tin-oxide (ITO)–glass substrate whose temperature was controlled by a thermoelectric element. As noted above, rather than driving $\mu_1(t)$ by solvent evaporation, instead monomers are continually delivered to the liquid layer from the gas phase, carried by an impinging laminar stream of high-purity nitrogen gas containing tetracene vapor generated in a heated crucible. This results in a well-controlled and spatially uniform driving force for crystallization, the rate of which can be varied by changing the flux [Fig. 1(a)]. The flux rate is computed from the induction time (i.e., the lag between the onset of deposition and first appearance of crystals), based on knowledge of the solvent layer thickness and critical supersaturation concentration (details are given in [34]). We chose this method for driving $\mu_1(t)$ for the higher degree of control it affords over the driving rate $d[\mu_1(t)]/dt$ and because the liquid layer thickness and temperature remain constant, simplifying the analysis.

Once the concentration of TET becomes high enough, small crystals nucleate in the solvent, adopting stationary positions as a result of pinning capillary forces. This gives each crystal a well-defined and fixed separation from its neighbors. Nucleation was monitored *in situ* by epifluorescence videomicroscopy, enabling detection of crystallites as small

as $\sim 1 \, \mu m^2$ in area [Fig. 1(b) and Fig. S1 in [34]]. Videos were then analyzed to determine the nucleation coordinates and time of formation of each crystal for a range of flux rates at a single temperature. Though rare, very small crystals were occasionally observed to be mobile in the liquid, consistent with (though not proof of) the assumption of homogeneous nucleation made in the development of the model above.

Because the solvent layer was very thin, the time scale for mixing throughout the thickness of the liquid $\tau_{\mathrm{mix}} = d_s D^{-1/2} \sim 10^{-2}$ s is essentially instantaneous on the time scale of the experiment, which lasts $\sim 10^2$ s. Here $d_s = 100$ nm is the solvent thickness measured by ellipsometry and $D \approx kT/6\pi\eta a$ is the diffusivity of TET in squalane (k is Boltzmann's constant, $T = 60\,°C$ is the substrate temperature, $\eta = 7.87$ mPa s is the viscosity [35], and $a = 4.09 \times 10^{-10}$ m is the molecular radius of TET [36]). Note that, since $d_s/a \gg 1$, the contribution of the solid substrate to the Stokes drag in these thin films is negligible, leading to bulklike isotropic Brownian diffusion [37]. The solvent layer thickness was also much less than the separation between crystals. The concentration can thus be considered essentially uniform throughout the thickness of the solvent, though spatially varying within the substrate plane, as discussed below.

A representative epifluorescence micrograph showing a typical film is presented in Fig. 1(b). Tetracene crystals are visible as bright rod-shaped features. X-ray-diffraction measurements performed on films after solvent removal agreed with TET's reported crystal structure and showed random in-plane but uniform out-of-plane alignment, with the (001) crystal plane parallel to the ITO substrate (Fig. S2 in [34]). High-resolution polarized optical microscopy images indicate the majority are single crystals, undergoing uniform extinction upon sample rotation when viewed between crossed polarizers (Fig. S3 in [34]). Crystals grow with thin prismatic morphologies, reaching an eventual size of 10–100 μm in length and 100–150 nm in thickness as measured by atomic force microscopy, about equal to the thickness of the liquid solvent layer. The observed growth habit is much less compact than the predicted equilibrium barrel morphology and more elongated than the predicted growth morphology, which is platelike, based on shape simulations from molecular binding energies [38–40]. Films prepared at significantly lower flux rates than those reported here included a higher proportion of crystals with platelike morphologies, suggesting that the elongated shape is kinetically influenced. The (001) form dominates all others, comprising $\sim 97\%$ of total crystal surface area. Growth of this form is very slow and limited to dislocations except at very high driving forces [39].

We are interested in comparing the time evolution of the experimentally measured nucleation rate dN/dt and crystal density $N(t)$ to Eqs. (1). Each is readily determined simply by counting the number of crystals in each video frame. The results are shown in Fig. 2 for films prepared using several different flux rates, where the origin on the time axis corresponds to the onset of monomer flux, initiated by opening a shutter. Three distinct regimes may be identified [26]: (i) There was an induction regime between the onset of deposition and the first appearance of crystals. Its duration depended on F (i.e., on both the areal flux rate and the solvent layer thickness), being shorter for higher rates. Since the
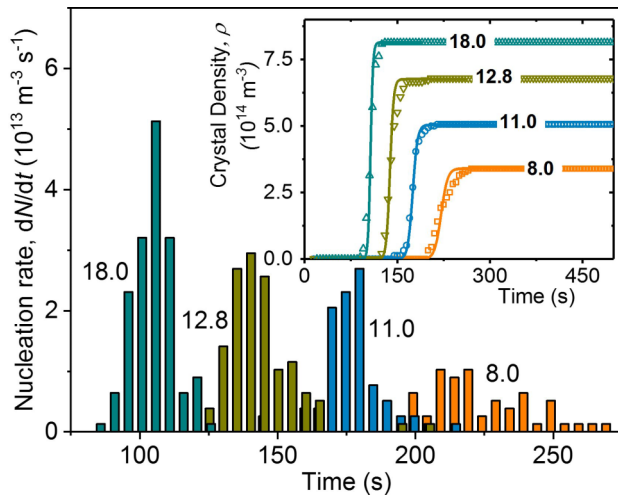
FIG. 2. Time-dependent nucleation rate for TET films prepared using four different flux rates. The flux in units of 10^{21} monomers m^{-3} s^{-1} is indicated for each sample. Nucleation occurs in a brief burst, preceded by an induction regime and followed by a growth regime. The inset shows the time evolution of the number of crystals per unit area. Solid lines result from fitting using Eqs. (1).

smallest crystal that could be detected was $\sim 1 \, \mu m^2$ in area and since during the nucleation regime crystals grew in size at a rate of $\sim 10 \, \mu m^2 \, min^{-1}$, the induction time coincided to within ~ 6 s with the first appearance of crystals in the video images, which were acquired in 5-s intervals. (ii) The induction regime was followed by a nucleation regime during which all crystals formed in a narrow time interval lasting 30–60 s. In terms of 2D coverage, the projected fractional surface area occupied by crystals was $\sim 1\%$ at the peak nucleation rate, increasing to $\sim 2\%$ by the time nucleation ceased. (iii) The nucleation regime was followed by a growth regime during which crystals increased in size but no new crystals formed.

The solid-line fits in the inset of Fig. 2 were obtained by numerical integration of Eqs. (1), using experimental values for all the relevant parameters ($n_0 = 3.36 \times 10^{23} \, m^{-3}$, $a = 4.09 \times 10^{-10} \, m$, $D = 7.58 \times 10^{-11} \, m^2 \, s^{-1}$, and $T = 333$ K). Fits were obtained by varying the Smoluchowski correction parameter γ and the surface energy σ, which are challenging to independently measure experimentally.[1] This gave (in order of increasing flux) $\sigma = 24 \, mN \, m^{-1}$ and $\gamma = 13.6$, $\sigma = 24 \, mN \, m^{-1}$ and $\gamma = 12.6$, $\sigma = 23 \, mN \, m^{-1}$ and $\gamma = 11.9$, and $\sigma = 23 \, mN \, m^{-1}$ and $\gamma = 14.4$, respectively. The independently fit Smoluchowski coefficients and surface energies are thus very consistent between independent experiments and essentially independent of F, as expected. To compare

the experimentally measured critical concentration c^* to the critical concentration n^* implied by solving the MFREs, we define the latter as being the concentration at which the nucleation rate becomes high enough to produce an average of one crystal per video frame (i.e., every 5 s) within a volume of solvent equal to that visible within the observation area ($1.56 \times 10^{-13} \, m^3$). Using this definition, the average critical concentration determined from the fits in Fig. 2 is $n^* = (2.1 \pm 0.3) \times 10^{24} \, m^{-3} = 3.5$ mM, again essentially independent of F, which compares to the experimental value $c^* = (1.6 \pm 0.2) \times 10^{24} \, m^{-3} = 2.7$ mM. Equations (1) are thus able to quantitatively capture all the major features of nucleation in these films, including the existence and duration of the induction, nucleation, and growth regimes, and the flux dependence of the nucleation rate, onset time of nucleation, and limiting crystal density at high coverage.

Before proceeding to discuss application of the model to the treatment of crystal spacing statistics, it is instructive to examine the action of the concentration $P(i^*, n)$ and i^* during the time integration of Eqs. (1). The integration is done numerically, updating the monomer and stable crystal concentrations, as well as the critical cluster concentration and the critical size, at each time step. The characteristic burst of nucleation seen in Fig. 2 arises from the interplay of i^* and $P(i^*, n)$; at low monomer density (but still maintaining supersaturation with $n > n_0$) the critical size is large and thus $P(i^*, n) \approx 0$ and the nucleation rate [given by $KP(i^*, n)n$] is suppressed. In this case, the monomer density increases linearly with flux. As the monomer density increases, i^* decreases and eventually $P(i^*, n)$ increases sharply, triggering a burst of nucleation. Following nucleation, the uptake of monomers by stable crystals [governed by the third term on the right-hand side of Eq. (1a)] becomes appreciable and the critical size again increases, accompanied by a corresponding decrease in the concentration of clusters of size i^*, and nucleation is once again arrested. The evolution of the critical cluster size and concentration with time are shown in Fig. 3, using the same parameters as Fig. 2. The general behaviors described above are evident: The nucleation regime is demarcated by a minimum in the critical size and a corresponding maximum of the critical concentration. Several other features are also apparent. Since the nucleation rate is proportional to P, we see that the origin of the flux dependence of the limiting crystal density N_{max} stems from the increase in the maximum P_{max} with flux. In addition, the width of the critical size concentration peak decreases markedly with increasing flux and therefore the nucleation regime becomes shorter in duration, resulting in a more rapid increase in N with increasing flux. The same behavior is also observed in the experimental results of Fig. 2.

According to the results in Fig. 3, the critical nucleus size at the onset of nucleation (i.e., at $n = n^*$) is $i^* \approx 59$ monomers for all four flux rates studied, close to the previously reported minimum critical size of TET in the organic solvent bis(2-ethylhexyl)sebecate ($i^* \approx 53$) [26]. This may be compared to the critical nucleus size of TET in vacuum-deposited films, which was estimated to be $i^* \approx 3$ on bare SiO$_2$ [41] and to that of structurally similar compounds such as pentacene [$i^* \approx 6$ on Si(001)] [42] and sexithiophene [$i^* \approx 5$ on H-terminated Si(100)] [43]. Thus i^* is consistently about an order

---

[1]The squalane-TET interfacial energy for a bulk film was measured by contact angle goniometry and found to be $5 \pm 10 \, mN \, m^{-1}$ (details are given in [34]). This measurement was made at room temperature on a planar TET film prepared by vacuum deposition and may not be representative of the interfacial energy of a nanoscale TET cluster of size $i^* \sim 10$–100 monomers in TET-saturated squalane at $60 \, °C$– the conditions under which nucleation occurs. For this reason we elected to include σ as a fitting parameter in the treatment of the data in Fig. 2.

FIG. 3. Critical nucleus size $i*$ (left axis) and the concentration of critical clusters $P(i*,n)$ (right axis) as functions of time, obtained from solving Eqs. (1)–(3) using the same parameters as in Fig. 2. The flux in units of 10^{21} monomers m^{-3} s^{-1} is indicated for each calculation. Note the correspondence of a minimum in critical cluster size with a maximum in the concentration of critical clusters, the driver of burst nucleation.

of magnitude larger in the liquid solvent environment than in vacuum.

III. MODELING DOMAIN SPACING STATISTICS

We next show how the model can be used to understand another important nanoscale morphological property of solution-processed polycrystalline films, namely, the relative spatial separation of crystalline domains. A close examination of images such as the one in Fig. 1 indicates that the positions of crystals are not entirely random in these films; rather they tend to be more widely separated than would be expected for complete spatial randomness (CSR), i.e., a 2D Poisson point process [44]. This effect is illustrated more clearly in Fig. 4, which shows the evolution of the mean nearest-neighbor spacing $\bar{d}_{NN}$ as a function of crystal density ρ (crystals μm^{-2}) during the nucleation regime for the same four flux rates examined above. Each symbol type in Fig. 4 represents a different flux rate, all of which fall onto a single universal curve. Initially, when few crystals have formed and they are widely separated, their spacing statistics agree with a random distribution $\bar{d}_{NN}^{CSR} = 1/(2\sqrt{\rho})$ (solid line in the main part of Fig. 4). As the density increases however, $\bar{d}_{NN}$ begins to deviate from $\bar{d}_{NN}^{CSR}$, eventually exceeding it by about 20% when nucleation finally ceases at the highest flux. The inset compares the experimental and CSR mean nearest-neighbor spacing probability distributions at the end of the nucleation regime for one particular film ($F = 18.0 \times 10^{21}$ μm^{-3} s^{-1}). The CSR distribution is given by $P_{CSR}(r)dr = 2\pi r\rho e^{-\pi\rho r^2} dr$, where r is the radial distance and $\rho_{av} = 8.1 \times 10^{-5}$ mm^{-2} is the average areal density of crystallites. Compared to the CSR model, the experimental distribution is skewed toward larger nearest-neighbor spacing and no crystals are observed to form closer than about 25 μm from their nearest neighbor. The distributions produced by other flux rates are qualitatively similar.
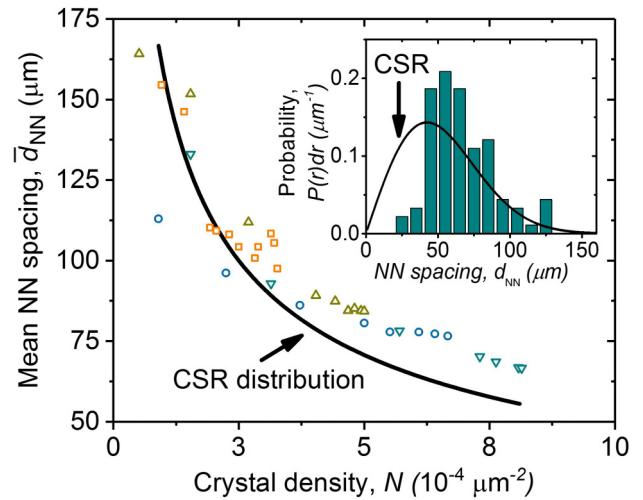
FIG. 4. At the beginning of the nucleation regime, the first crystals to become visible are randomly positioned with nearest-neighbor (NN) spacing close to a CSR (2D Poisson) distribution (line). As the density increases, the mean NN spacing remains larger than that predicted by the 2D Poisson distribution, indicating suppressed nucleation in the vicinity of crystals that have already formed due to competition for monomers. Squares denote $F = 8.0 \times 10^{21}$ m^{-3} s^{-1}; circles, $F = 11.0 \times 10^{21}$ m^{-3} s^{-1}; upward triangles, $F = 12.8 \times 10^{21}$ m^{-3} s^{-1}; and downward triangles, $F = 18.0 \times 10^{21}$ m^{-3} s^{-1}. The inset compares the experimental (bars) and Poisson (line) NN spacing probability distributions at the end of the nucleation regime for $F = 18.0 \times 10^{21}$ m^{-3} s^{-1}.

The trends in Fig. 4 indicate that nucleation is suppressed near crystals that have already formed, a well-known consequence of diffusion-mediated competition for growth units [45]. The effects are shown clearly in the radially averaged crystal separation probability distribution $\rho(r)$ equal to the probability of observing a crystal separated by distance r from another crystal (Fig. 5). In Refs. [46,47] Evans and Bartelt postulated a radial probability distribution for 2D island nucleation in vacuum-deposited films of the form

$$\rho(r) = J[n(r)]/J[n(r = \infty)], \tag{5}$$

where the nucleation rate J is proportional to

$$J \propto n(r)^{i*+1}, \tag{6}$$

using the Walton relation. We utilize the main ideas of this approach here, but modify the details to account for the concentration-dependent critical nucleus size and the kinetics of nucleation in a supersaturated solvent.

Equation (5) equates the probability of observing a crystal at a distance r from a given crystal with the nucleation rate at r, itself a function of the monomer concentration at that distance $n(r)$. We note that the function $n(r)$ is the position-dependent monomer density, measured with respect to a crystal center, in contrast to the monomer and crystal densities calculated via Eqs. (1a) and (1b), which are average (mean-field) quantities. For the discussion here, we define this average monomer density as $n(r = \infty) = \langle n \rangle$. The function $n(r)$ may be constructed by solving the appropriate diffusion equation for monomers in the presence of a (constant) flux and an island sink. The problem is made tractable by careful consideration of
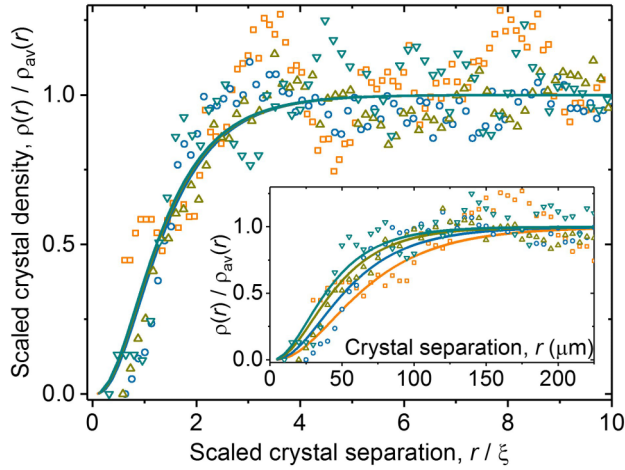
FIG. 5. Comparison of the experimental crystal separation probability distribution to the predicted distribution given by the treatment described in the text (solid lines). The inset shows the unscaled distribution. Squares denote $F = 8.0 \times 10^{21}$ m^{-3} s^{-1}; circles, $F = 11.0 \times 10^{21}$ m^{-3} s^{-1}; upward triangles, $F = 12.8 \times 10^{21}$ m^{-3} s^{-1}; and downward triangles, $F = 18.0 \times 10^{21}$ m^{-3} s^{-1}. Line color is matched to symbol color.

the boundary condition on $n(r)$ as $r \to \infty$, where the solution for $n(r = \infty) = \langle n \rangle$ is governed by Eqs. (1a) and (1b), which will be elucidated in detail below.

The appropriate diffusion equation is given by

$$\frac{\partial n(r)}{\partial t} = D\nabla^2 n(r) + F - D\xi^{-2} n(r), \qquad (7)$$

where D is the monomer diffusion constant, ξ is a characteristic diffusion length, and F is the flux rate [we note that we have explicitly restricted the regime to low crystal coverage, since the flux rate in Eq. (7) refers to the flux of monomers into the free solvent, as opposed to impinging upon nucleated islands]. In the limit of $r \to \infty$, Eq. (7) must recover Eq. (1a); in this case, then, direct comparison yields, utilizing the definition of the collision kernel K,

$$\xi^{-2} = (4\pi a i^{*\frac{1}{3}})[P(i,n) + \langle N \rangle]. \qquad (8)$$

To further simplify this result, we note that Eq. (7) will be solved in the physically relevant nucleation regime, when the local kinetics involve the processes of flux, nucleation, and growth, and therefore the local-density variations are most significant. In the nucleation regime, $P \approx P(i^*, n_{\max})$, where $n_{\max}$ is the peak in the monomer density (just after the onset of nucleation) from Eq. (1a), and $\langle N \rangle \approx \frac{1}{2} N_{\max}$, where $N_{\max}$ is the final crystal density following cessation of nucleation. From the numerical solutions to (1a) and (1b), we find that under these conditions (see Figs. 2 and 3) $\langle N \rangle \gg P(n_{\max}, i^*)$ and Eq. (8) simplifies to $\xi^{-2} \approx (2\pi a i^{*\frac{1}{2}}) N_{\max}$.

In order to proceed to a tractable (analytic) solution to Eq. (7), we insert Eq. (8) into Eq. (1a) and subtract (1a) from (7), viz.,

$$\frac{\partial}{\partial t}[n(r) - \langle n \rangle] = D\nabla^2[n(r) - \langle n \rangle] - D\xi^{-2}[n(r) - \langle n \rangle] \approx 0, \qquad (9)$$

where, in the final step, we make the simplifying assumption that time-varying deviations of the local density from the average value are negligible [48]. In the present case, this is largely justified by the fact that in the nucleation regime, $\langle n \rangle$ is near a peak and its time derivative is therefore zero; since $\langle n \rangle$ drives the time dependence of the overall concentration, the simplification is a reasonable approximation.

Solving Eq. (9) requires a boundary condition on the monomer concentration at the crystal boundary, that is, $n(r = R)$, with R the radius of (an assumed) circular crystal. The value $n(r = R)$ is given by a dynamic equilibrium at the crystal boundary. Since nucleation and growth are taking place in a supersaturated solution under a constant flux of fresh monomers, this boundary concentration must lie between the saturation concentration n_0 and the critical concentration n^*. In particular, the value $n(r = R)$ is set by the equilibrium between uptake of monomers by a crystal and addition of monomers at rate F, which may be obtained from the rate equations (1a) and (1b). In the growth regime following the cessation of nucleation, the crystal density is constant, $\langle N \rangle = N_{\max}$, and the nucleation rate is zero, $\frac{dN}{dt} = 0$. Equation (1a) then becomes $\frac{d\langle n \rangle}{dt} = F - K_{eq} N_{\max} \langle n \rangle$, where $K_{eq} = 4\pi\gamma D(i^*)^{\frac{1}{3}}$ is the rate for the uptake of monomers at equilibrium. Here K_{eq} is computed using the value of i^* given by the critical monomer concentration n^* at the onset of nucleation, based on the experimentally observed nucleation time t^* and flux rate. This equation has the solution $n_{eq} = \frac{F}{K_{eq} N_{\max}} + ce^{-K_{eq} N_{\max} t}$, so at long times the equilibrium value for the monomer density is given by $n_{eq} = \frac{F}{K_{eq} N_{\max}}$. During the nucleation regime, we use this concentration for the boundary condition $n(r = R)$.[2] With this, the solution to Eq. (9) is given (in plane polar coordinates) by

$$n(r) = \langle n \rangle + (n_{eq} - \langle n \rangle)\frac{K_0\left(\frac{r}{\xi}\right)}{K_0\left(\frac{R}{\xi}\right)}, \qquad (10)$$

where K_0 is the modified Bessel function of order zero and the crystal radius R is taken to equal the radius of a critical nucleus, found from Eq. (4): $R = a[i^*(n = n^*)]^{\frac{1}{3}}$. In addition, $\langle n \rangle$ is set equal to the average monomer concentration during the nucleation regime, found during the numerical integration of Eqs. (1). Equation (10) may then be used to produce the predicted function $\rho(r)$, from Eq. (5), with the nucleation rate given explicitly by Eq. (1b):

$$J = \frac{dN}{dt} = K P[i^*, n(r)] n(r)$$

$$= \gamma 4\pi a (i^*)^{\frac{1}{3}} D n(r)^2 \left(\frac{n(r)}{n_0}\right)^{i^*-1}$$

$$\times \exp\left[\frac{-4\pi\sigma a^2(i^{*\frac{2}{3}} - 1)}{kT}\right], \qquad (11)$$

where i^* is again concentration dependent and given by Eq. (4).

_____

[2]This assertion has been checked by simulation of the full diffusion equation (7) via finite-difference grid methods and found to be exact in this case.

Figure 5 shows that this treatment provides a remarkably accurate *prediction* of the crystal spacing statistics in these TET films over the full range of studied flux rates. The solid lines were computed for each flux rate using Eq. (11), along with the experimentally measured saturation and critical concentrations n_0 and n^*, and effective interfacial energy σ determined from the MFRE treatment of the nucleation rate discussed above. Thus on the basis of the time-dependent nucleation rate alone, the radial distribution function can be accurately predicted. Consistent with Eq. (10), the distributions for different flux rates collapse to a single universal curve when scaled by ξ, which establishes a characteristic length scale for the mesoscale structure of these polycrystalline films. Nucleation is inhibited at distances $\leqslant \sim 3\xi$ from existing crystals, equal to about 1.4 times the average nearest-neighbor spacing (for comparison, the prediction from the CSR model gives unity probability for all crystal spacings, in strong disagreement with the experimental observation). These results demonstrate that the spacing distribution follows a predictable universal scaling caused by a local depletion of the monomer concentration around growing crystals, the effects of which are quantitatively captured by accounting for diffusion using boundary conditions consistent with the MFRE treatment of Eqs. (1).

IV. DESIGN RULES FOR PROGRAMMING NANOSCALE MORPHOLOGY

Finally, to generalize these results to other systems, we numerically evaluated Eqs. (1) and (11) over a range of parameter values to explore the effects of changing experimental conditions. As shown in Figs. 6 and 7, this reveals a set of systematic relationships serving as design rules to guide the selection of experimental conditions producing films with targeted morphologies. We examined the effects of F, D, γ, and D/F on the final number of crystals $N_{\max}$ formed per unit volume by the end of the nucleation regime, as well as a measure of the crystal spacing distribution, which we characterize by the mean scaled distance $r_{1/2}$ at which $\rho(r) = \rho(r = \infty)/2$. The quantity $r_{1/2}$ can be thought of as a nucleation exclusion distance, i.e., the length scale characterizing the tendency of crystals to avoid nucleating near one another. As shown in Figs. 6 and 7, this leads to a set of relationships that turn out to be well described by power-law scalings:

$$N_{\max} \sim F^v, \tag{12a}$$

$$N_{\max} \sim D^w, \tag{12b}$$

$$N_{\max} \sim \gamma^x, \tag{12c}$$

$$N_{\max} \sim \left(\frac{D}{F}\right)^y, \tag{12d}$$

$$r_{1/2} \sim \xi \sigma^z, \tag{12e}$$

where $v \approx 0.99$ and w, x, and $y \approx -0.99$. The results in Figs. 6 and 7 are obtained by solving Eqs. (1) and (11) numerically, with all parameters save the variable of interest held constant, a process that is then repeated for different combinations of variables. Numerical solutions are necessary because the
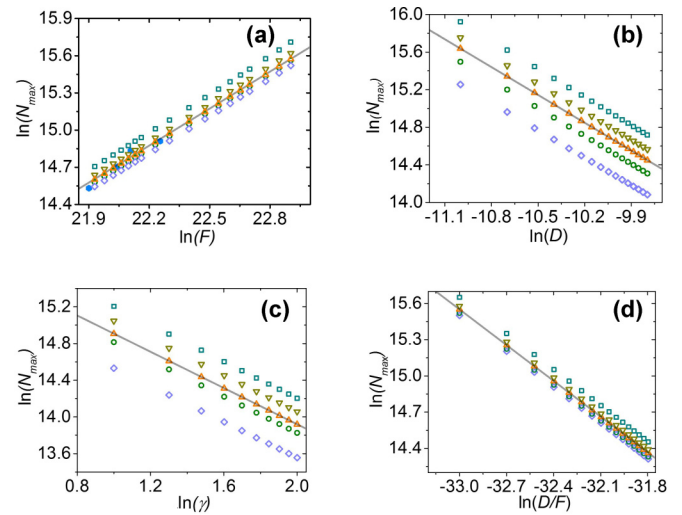
FIG. 6. Scaling behavior of $N_{\max}$ determined from numerical integration of Eqs. (1). Lines are a power-law fit to a representative series in each set, chosen to correspond to the average parameters found from experiment. For each figure part and symbol type the parameters are given as $\{\sigma\,(\mathrm{N\,m^{-1}}),\ \gamma\,(\mathrm{unitless}),\ D\,(\mathrm{m^2\,s^{-1}}),\ F\,(\mathrm{m^{-3}\,s^{-1}})\}$ as follows: (a) squares $\{0.017, 18.0, 7.58 \times 10^{-11}, \text{variable}\}$, downward triangles $\{0.021, 13.0, 7.58 \times 10^{-11}, \text{variable}\}$, upward triangles $\{0.0235, 13.0, 7.58 \times 10^{-11}, \text{variable}\}$, circles $\{0.0205, 18.0, 7.58 \times 10^{-11}, \text{variable}\}$, diamonds $\{0.021, 18.0, 7.58 \times 10^{-11}, \text{variable}\}$, and solid hexagons are experimentally measured values; (b) squares $\{0.013, 13.0, \text{variable}, 1.05 \times 10^{22}\}$, downward triangles $\{0.021, 10.0, \text{variable}, 1.05 \times 10^{22}\}$, upward triangles $\{0.021, 13.0, \text{variable}, 1.05 \times 10^{22}\}$, circles $\{0.021, 18.0, \text{variable}, 1.05 \times 10^{22}\}$, and diamonds $\{0.03, 13.0, \text{variable}, 1.05 \times 10^{22}\}$; (c) squares $\{0.012, \text{variable}, 7.58 \times 10^{-11}, 1.05 \times 10^{22}\}$; downward triangles $\{0.021, \text{variable}, 7.58 \times 10^{-11}, 1.45 \times 10^{22}\}$, upward triangles $\{0.021, \text{variable}, 7.58 \times 10^{-11}, 1.25 \times 10^{22}\}$, circles $\{0.0205, \text{variable}, 7.58 \times 10^{-11}, 8.5 \times 10^{21}\}$, and diamonds $\{0.03, \text{variable}, 7.58 \times 10^{-11}, 1.05 \times 10^{22}\}$; and (d) squares $\{0.017, 18.0, \text{variable}, \text{variable}\}$, downward triangles $\{0.021, 16.0, \text{variable}, \text{variable}\}$, circles $\{0.0205, 18.0, \text{variable}, \text{variable}\}$, and diamonds $\{0.021, 18.0, \text{variable}, \text{variable}\}$.
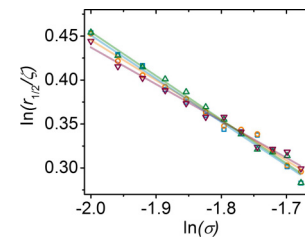
FIG. 7. Scaling behavior of $r_{1/2}$ with σ at various flux rates. For each symbol type the parameters are given as follows $\{\gamma\,(\mathrm{unitless}),\ D\,(\mathrm{m^2\,s^{-1}}),\ F\,(\mathrm{m^{-3}\,s^{-1}}),\ F\,(\mathrm{unitless})\}$: circles $\{18.0, 7.58 \times 10^{-11}, 8.0 \times 10^{21}, -0.42\}$, squares $\{18.0, 7.58 \times 10^{-11}, 1.0 \times 10^{22}, -0.47\}$, upward triangles $\{18.0, 7.58 \times 10^{-11}, 1.0 \times 10^{22}, -0.47\}$ and $\{18.0, 7.58 \times 10^{-11}, 1.2 \times 10^{22}, -0.49\}$, and downward triangles $\{18.0, 7.58 \times 10^{-11}, 1.4 \times 10^{22}, -0.50\}$.

complexity of the relationships governing the critical nucleus size and the resulting density of clusters of size i^* make analytical expressions for the scaling behavior untenable without unreasonable approximations. The exponents v, w, x, and y are found to be essentially constant (within ± 0.02) over the full range of explored parameter space. As shown in Fig. 7, the exponent z, on the other hand, is not constant, but instead varies in a regular way between -0.4 and -0.6, depending on F and γ. The range of conditions over which these relationships apply encompasses a large parameter space of chemical properties and experimental conditions and should therefore apply to a wide range of organic crystalline materials, solvents, and growth conditions. Taken together, the scaling relationships in Eq. (12) define a set of design rules that can guide the selection of experimental conditions to tailor film morphologies for particular applications.

V. CONCLUSION

The performance of devices based on solution-processed molecular films is directly linked to their nanoscale polycrystalline structure, itself a function of the chemical characteristics and processing conditions employed in film preparation. We have presented an integrated model treating nucleation kinetics from quasi-2D supersaturated solvents, taking into account the supersaturation driving rate, the concentration dependence of the nucleation free-energy barrier, and diffusion-governed competition for monomers between nucleation and growth. Based on a small number of experimentally accessible inputs, the model produces quantitative predictions for the mean crystal density and predicts other morphological parameters such as the intercrystalline spacing statistics. The model is tested by comparison to nucleation and growth experiments on tetracene films deposited from squalane, with monomer concentration driven by a flux of tetracene vapor impinging on the solvent layer. Excellent agreement is demonstrated for the monomer concentration driving rate-dependent crystal density, intercrystalline spacing statistics, induction time, and nucleation rate. Finally, the model leads to a set of predictive design rules for solution-processed films useful for guiding the selection of experimental conditions to produce targeted nanoscale morphologies.

[1] G. R. Desiraju, *Crystal Engineering–The Design of Organic Solids* (Elsevier, New York, 1989).

[2] R. Farchioni and G. Grosso, *Organic Electronic Materials: Conjugated Polymers and Low Molecular Weight Organic Solids* (Springer Science + Business Media, New York, 2013), Vol. 41.

[3] M. Pope and C. E. Swenberg, *Electronic Processes in Organic Crystals and Polymers* (Oxford University Press, Oxford, 1999).

[4] F. Garnier, R. Hajlaoui, A. Yassar, and P. Srivastava, Science **265**, 1684 (1994).

[5] R. F. Service, Science **278**, 383 (1997).

[6] G. H. Gelinck *et al.*, Nat. Mater. **3**, 106 (2004).

[7] G. Horowitz, Adv. Mater. **10**, 365 (1998).

[8] M. E. Roberts, S. C. Mannsfeld, N. Queraltó, C. Reese, J. Locklin, W. Knoll, and Z. Bao, Proc. Natl. Acad. Sci. USA **105**, 12134 (2008).

[9] T. Sekitani, T. Yokota, U. Zschieschang, H. Klauk, S. Bauer, K. Takeuchi, M. Takamiya, T. Sakurai, and T. Someya, Science **326**, 1516 (2009).

[10] M. Kaltenbrunner *et al.*, Nature (London) **499**, 458 (2013).

[11] T. Sekitani, M. Takamiya, Y. Noguchi, S. Nakano, Y. Kato, T. Sakurai, and T. Someya, Nat. Mater. **6**, 413 (2007).

[12] C. J. Brabec and J. R. Durrant, MRS Bull. **33**, 670 (2008).

[13] J. G. Laquindanum, H. E. Katz, A. J. Lovinger, and A. Dodabalapur, Chem. Mater. **8**, 2542 (1996).

[14] T. Minakata, H. Imai, M. Ozaki, and K. Saco, J. Appl. Phys. **72**, 5220 (1992).

[15] A. J. Lovinger, H. E. Katz, and A. Dodabalapur, Chem. Mater. **10**, 3275 (1998).

[16] A. J. Mäkinen, A. R. Melnyk, S. Schoemann, R. Headrick, and Y. Gao, Phys. Rev. B **60**, 14683 (1999).

[17] Y. Huang, E. J. Kramer, A. J. Heeger, and G. C. Bazan, Chem. Rev. **114**, 7006 (2014).

[18] E. Silins and V. Capek, *Organic Molecular Crystals: Interaction, Localization, and Transport Phenomena* (American Institute of Physics, New York, 1994).

[19] N. Karl, in *Crystals—Growth, Properties and Applications*, edited by H. C. Freyhardt (Springer, New York, 2001).

[20] C. D. Dimitrakopoulos and P. R. Malenfant, Adv. Mater. **14**, 99 (2002).

[21] Y. Diao, L. Shaw, Z. Bao, and S. C. Mannsfeld, Energ. Environ. Sci. **7**, 2145 (2014).

[22] S. R. Forrest, Nature (London) **428**, 911 (2004).

[23] R. J. Davey, S. L. Schroeder, and J. H. ter Horst, Angew. Chem. Int. Ed. Engl. **52**, 2166 (2013).

[24] D. Walton, J. Chem. Phys. **37**, 2182 (1962).

[25] L. A. Morrison, D. Stanfield, M. Jenkins, A. A. Baronov, D. L. Patrick, and J. M. Leger, Org. Electron. **33**, 269 (2016).

[26] A. Baronov, K. Bufkin, D. W. Shaw, B. L. Johnson, and D. L. Patrick, Phys. Chem. Chem. Phys. **17**, 20846 (2015).

[27] M. V. Smoluchowski, Z. Phys. Chem. **92**, 129 (1917).

[28] S. L. Girshick and C. P. Chiu, J. Chem. Phys. **93**, 1273 (1990).

[29] S. L. Girshick, J. Chem. Phys. **94**, 826 (1991).

[30] J. Venables, Philos. Mag. **27**, 697 (1973).

[31] J. Venables, G. Spiller, and M. Hanbucken, Rep. Prog. Phys. **47**, 399 (1984).

[32] D. T. Robb and V. Privman, Langmuir **24**, 26 (2008).

[33] S. Karthika, T. Radhakrishnan, and P. Kalaichelvi, Cryst. Growth Des. **16**, 6663 (2016).

[34] See Supplemental Material at http://link.aps.org/supplemental/10.1103/PhysRevMaterials.1.043404 for an additional description of the experimental apparatus and film characterization (x-ray diffraction and polarized optical microscopy) and determination of the flux rate, solvent viscosity, and TET solubility.

[35] H. Wedershoven, C. Berendsen, J. Zeegers, and A. Darhuber, Appl. Phys. Lett. **104**, 054101 (2014).

[36] D. Holmes, S. Kumaraswamy, A. J. Matzger, and K. P. C. Vollhardt, Chemistry—Eur. J. **5**, 3399 (1999).

[37] B. Lin, J. Yu, and S. A. Rice, Phys. Rev. E **62**, 3909 (2000).

[38] F. R. Massaro, M. Moret, M. Bruno, M. Rubbo, and D. Aquilano, Cryst. Growth Des. **11**, 4639 (2011).

[39] H. Cuppen, W. Graswinckel, and H. Meekes, Cryst. Growth Des. **4**, 1351 (2004).

[40] D. Nabok, P. Puschnig, and C. Ambrosch-Draxl, Phys. Rev. B **77**, 245316 (2008).

[41] J. Shi and X. R. Qin, Phys. Rev. B **78**, 115412 (2008).

[42] F.-J. Meyer zu Heringdorf, M. Reuter, and R. Tromp, Appl. Phys. A **78**, 787 (2004).

[43] M. Brinkmann, S. Graff, and F. Biscarini, Phys. Rev. B **66**, 165430 (2002).

[44] P. J. Clark and F. C. Evans, Ecology **35**, 445 (1954).

[45] S. Varma, C. Reaves, V. Bressler-Hill, S. DenBaars, and W. Weinberg, Surf. Sci. **393**, 24 (1997).

[46] M. C. Bartelt and J. W. Evans, Phys. Rev. B **46**, 12675 (1992).

[47] J. Evans and M. Bartelt, Surf. Sci. Lett. **284**, L437 (1993).

[48] G. S. Bales and D. S. Chrzan, Phys. Rev. B **50**, 6057 (1994).